



HAL
open science

Euclid flight H2RG IR detectors: per pixel conversion gain from on-ground characterization for the Euclid NISP instrument

Aurélia Secroun, Jean-Claude Clémens, Anne Ealet, William Gillard, Benoît Serra, Julien Zoubian, Rémi Barbier, Sylvain Ferriol, Bogna Kubik, Cyrille Rosset, et al.

► To cite this version:

Aurélia Secroun, Jean-Claude Clémens, Anne Ealet, William Gillard, Benoît Serra, et al.. Euclid flight H2RG IR detectors: per pixel conversion gain from on-ground characterization for the Euclid NISP instrument. SPIE Astronomical Telescopes + Instrumentation 2018, Jun 2018, Austin, United States. pp.1070921, 10.1117/12.2312518 . hal-01959780

HAL Id: hal-01959780

<https://hal.science/hal-01959780>

Submitted on 14 Feb 2019

HAL is a multi-disciplinary open access archive for the deposit and dissemination of scientific research documents, whether they are published or not. The documents may come from teaching and research institutions in France or abroad, or from public or private research centers.

L'archive ouverte pluridisciplinaire **HAL**, est destinée au dépôt et à la diffusion de documents scientifiques de niveau recherche, publiés ou non, émanant des établissements d'enseignement et de recherche français ou étrangers, des laboratoires publics ou privés.

Euclid flight H2RG IR detectors: per pixel conversion gain from on-ground characterization for the Euclid NISP instrument

Secroun A.^a, Barbier R.^b, Buton C.^b, Clémens J-C.^a, Conversi L.^d, Ealet A.^a, Ferriol S.^b, Fornari F.^e, Gillard W.^a, Kohley R.^d, Kubik B.^b, Rosset C.^c, Serra B.^a, Smadja G.^b, and Zoubian J.^a

^aAix Marseille Univ, CNRS/IN2P3, CPPM, Marseille, France

^bIPNL, CNRS, Lyon University, 4 rue E. Fermi, 69100 Villeurbanne, France

^cAPC, CNRS Paris Diderot University, Bat. Condorcet, 75205 Paris, France

^dESAC, ESA, Camino Bajo del Castillo, 28692 Villanueva de la Canada, Spain

^eIstituto Nazionale di Fisica Nucleare, Sezione di Bologna, Via Irnerio 46, Bologna 40126, Italy

ABSTRACT

Euclid is a major ESA mission for the study of dark energy planned to launch in 2021. Euclid will probe the expansion history of the Universe using weak lensing and baryonic acoustic oscillations probes. A survey of 15,000 deg² of the sky with the instrument NISP (Near-Infrared Spectro-Photometer), in the 900 – 2100 nm band, will give both the photometric and spectrometric redshifts of tens of millions of galaxies. The 16 H2RG detectors of the NISP focal plane array are still being characterized at CPPM (Marseille). Already 16 out of 20 flight detectors have been tested and a straightforward analysis done. Performance of the dedicated test benches – in particular control of flux and temperature – as well as an overview of the test flow will be presented. This paper will present methods and some preliminary results on two detectors focusing on the determination of a per pixel conversion gain.

Keywords: Euclid, NISP, IR detectors, H2RG, Conversion factor, Conversion gain, Telemetry

1. INTRODUCTION

Euclid is a major ESA mission due to launch in 2021 aimed at mapping the geometry of the dark Universe. Euclid is optimized for two probes, weak gravitational lensing and baryonic acoustic oscillations,¹ which will be measured thanks to a visible imager (VIS) and an infrared spectrometer and photometer (NISP) both designed and built by the Euclid Consortium teams. The NISP instrument² will hold a large focal plane array of 16 near-infrared H2RG detectors which are a key element to the performance of the NISP, and therefore to the science return of the mission. Thorough on-ground testing of the detectors has started at CPPM since June 2017 for characterization and calibration purposes with a view to producing a reference database of pixel maps of detector performances in terms of dark current, noise and quantum efficiency, among others. Most important characterization is on parameters such as persistence and non-linearity for which models should be defined on ground as they are difficult to characterize in flight. These will be addressed in a future paper.

Dedicated test benches as well as the whole acquisition and L1 level (Data Quality Checking) analysis codes have been previously designed, built and validated thanks to several pilot runs. This work has led to an efficient and reliable fully integrated acquisition and validation system and a thorough test flow whose main features are presented in the first part. The second part presents some first results and methods focusing on the derivation of a per pixel conversion gain for two detectors taken as an example.

Further author information: Send correspondence to Aurélie Secroun
E-mail: secroun@c ppm.in2p3.fr, Telephone: +33 (0)4 91 82 72 15

2. CHARACTERIZATION OF H2RG DETECTORS

Characterization has been going on continuously for more than a year at CPPM. Detectors are tested four by four in two twin test benches specifically designed and fabricated for the purpose of detector characterization. Characterization is closely linked to the NISP instrument calibration both on ground and in flight since detectors are a major part of the instrument chain. Its aim is to provide pixel maps of detector performance that will allow the mission to reach 1% accuracy on the galaxy measured flux after correction. Thanks to a fully automated chain of acquisition and a thorough flow of tests developed between IPNL (in charge of acquisition software) and CPPM (in charge of setup), some 20 TB of data are acquired for each detector with an average of 85% efficiency in acquisition time.

2.1 Detectors

The focal plane of the NISP instrument holds 16 H2RG detectors specifically designed for the Euclid mission with a $2.3 \mu\text{m}$ cutoff and $18 \mu\text{m}$ pixel pitch. These detectors have been procured and qualified by NASA following a ranking done in collaboration with the Euclid Consortium Detector Scientist. For the purpose of characterization, the detectors are readout by sidecar cold electronics (SCE) provided by Teledyne and Markury Scientific EGSE which allows simultaneous readout of two detectors (and potentially up to 16 as will be tested on the NISP instrument).

Their configuration includes 15 dB gain and 500 mV bias voltage to optimize dynamic range according to Euclid needs. In particular, the saturation of ADC voluntarily takes place before the saturation of full well. The matrix is readout through 32 channels. Reference pixel correction has been defined and optimized previously in order to minimize noise.⁴

Among the 16 detectors, two of them are used as an example to show some methods and results. Their flat field illuminations are shown in figure 1 where singular patterns may be observed. Dark currents at the level of 10^{-3} e/s have been measured as may be seen in table 1.

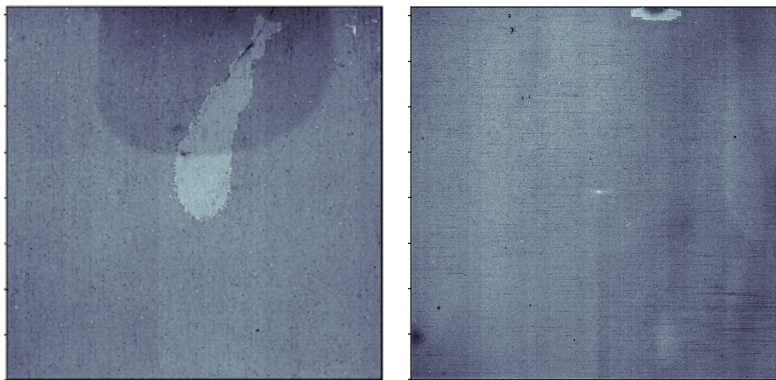


Figure 1. Flat field illumination shows a “fish-shape” on scs1 [left] and a small “oval” on scs2 [right].

Table 1. Dark current and noise at 85K

| | scs1 | scs2 |
|-----------------------|----------------------|----------------------|
| Dark current [median] | 0.006 e/s | 0.010 e/s |
| CDS noise [median] | 18.90 e (9.96 ADU) | 15.98 e (8.74 ADU) |

(Assuming a gain of 0.50 for scs1 and 0.51 ADU/e for scs2)

2.2 Test flow

Four types of acquisitions allow to evaluate the detector performance: tests in dark condition for dark current and science mode noises (photometry and spectroscopy), tests under changing flux illumination to study non-linearity and persistence, tests under changing wavelength illumination to derive flat fielding maps, and electrical tests to sort out non-linearity of the detector from that of the ASICs.

Most tests are done at three temperatures since the flight operating temperature is not known precisely yet: 80K, 85K and 90K (dark tests are also done at 100K). This will allow to adjust the calibration to the onboard operating temperature thanks to the derivation of temperature dependent models of various parameters, such as dark current and persistence. Herein presented results are derived at 85K.

To evaluate conversion factor, illumination with changing flux of various types may be used: alternate flux and short dark, alternate flux and long dark, alternate flux and “zodi”,* and continuous illumination. Illumination ramps are based on the spectroscopy mode of the NISP instrument, namely a duration of 560 seconds. These various illumination types should allow to decorrelate effects of trapping and detrapping competing within the pixels.

2.3 Test bench performance

Two parameters are particularly critical to the measurements done in the above described test flow: the thermal stability of the focal plane array which must be controlled to the mK in order to limit thermal effects and the stability and homogeneity of the flux received on the detector. The thermal stability of focal plane array has been checked to be better than 2mK.³

A Thorlabs 1600P LED (with 1550 nm central wavelength at room temperature) is used to provide homogeneous flux. Spatial homogeneity has been checked previously to better than 2%.³ Moreover, controlling current allows to vary the incoming flux from less than 1 e/s to more than 4000 e/s. The flux stability of LED is continuously monitored: a cooled reference photodiode directly faces the LED and measures its flux. A stability of better than 0.5% over the whole time of acquisition has been obtained. As may be seen in figure 2, the LED flux is stable to better than 0.1% over single acquisitions (duration of up to 15 hrs). On the contrary, detector response shows stronger variations during the first few ramps and it may be seen (dashed lines) that this variation is stronger for continuous-illumination acquisitions, up to 4%. This variation may be due to detrapping from the previous ramp. These effects are quite disturbing for the derivation of the conversion gain as will be seen below.

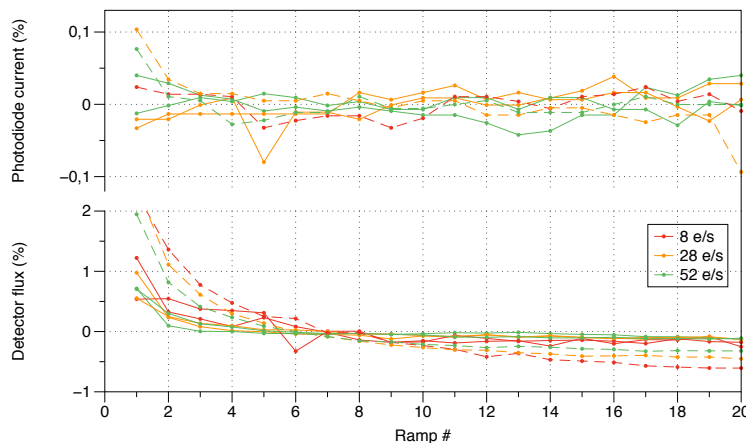


Figure 2. Photodiode [top] and detector [bottom] normalized relative flux responses for three typical incoming fluxes from the LED. Dashed lines correspond to continuous illumination, while continuous lines correspond to alternation of illumination and zodi or dark.

* “zodi” refers to a flux of 2 e/s equivalent to the zodiacal background that the NISP instrument will see onboard.

3. CONVERSION GAIN

To validate that the detector fulfills science requirements and derives actual fluxes from observed galaxies, measured signal should be expressed in physical terms (electrons or photons) rather than the arbitrary digital unit (ADU) that is the result from the analog-to-digital conversion (ADC) of the charge present in the photodiode. For that matter, the detector conversion gain or conversion factor must be evaluated precisely. For the Euclid mission it is a fundamental step in order to derive fluxes with 1% accuracy. Most of all, a pixel map of the gain should be produced if, as will be shown hereafter, it is not spatially homogeneous.

3.1 Method

Conversion gain is generally defined as the number of electrons represented by each ADU, and may be considered as the combination of two terms: the charge-to-voltage conversion (V/e) and the analog-to-digital conversion (ADU/V). Many methods have been derived to calculate the conversion gain among which the two main ones, which actually end up being mathematically equivalent, are the photon transfer^{5,6} and the mean variance.⁷ More recent works have also proposed solutions taking into account finer effects such as non-linearity⁸ or interpixel capacitance.^{9,10}

The standard “variance vs. signal” method is of interest for it allows to derive the conversion gain in the presence of read noise, which is the case at low fluxes, where our detectors are expected to be linear. This general method assumes a linear response of the detector, Poisson statistics of incident photons and negligible gain variance.

Then, the output signal S is given by

$$S \text{ (ADU)} = G \text{ (ADU/e)} \cdot N_e \text{ (e)} \quad (1)$$

where G is the conversion gain and N_e , the mean number of signal electrons, is supposed to follow Poisson statistics. Applying the quadratic propagation of errors, one may derive the conversion gain through:

$$\sigma_S^2 = G \cdot S + \sigma_R^2, \quad (2)$$

where G is the conversion gain (in ADU/e), S is the output signal (ADU), σ_S is the illumination dependent noise and σ_R represents illumination independent fluctuations (read noise). Thus with a simple least square fit, the gain may be obtained as the slope of the fit, while the read noise will come from the intercept of the fit.

Figure 3, left, shows the beginning of scs2 “variance vs. signal” curve for which several fluxes have been combined and seem to nicely align. Figure 3, right, shows the residual from the least square fit obtained for signals up to 4000 ADU. This method seems well adapted to our experiment and has been applied here to evaluate the conversion gain of the detectors.

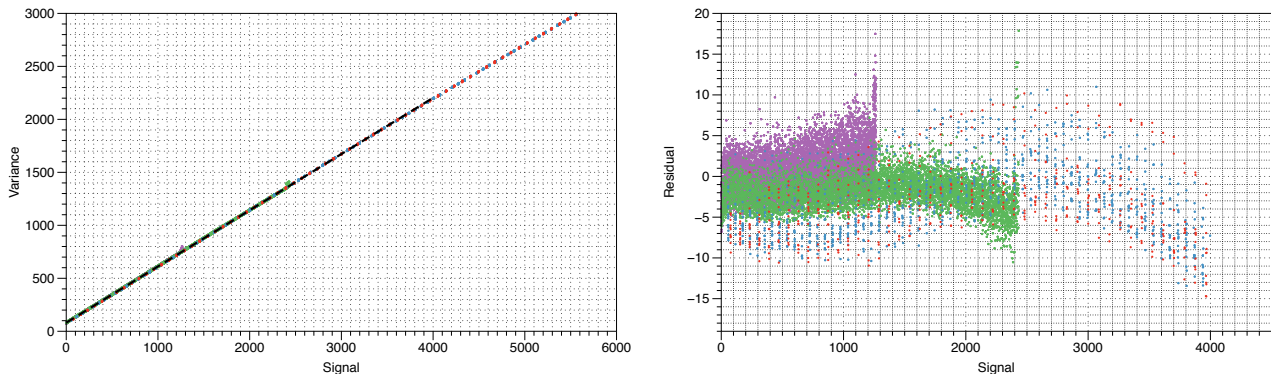


Figure 3. Variance vs. signal of scs2 [left] and residual from the least square fit [right]. Several fluxes and ramps of data are accumulated here [dots of various colors]. Fit is superimposed on the curve [black dashed line].

Experimentally, the conversion gain has been derived from pairs of ramps, referred to as “fast PTC” technique. While the standard technique requires to acquire N ramps at a number of fluxes between dark and saturation, here only two ramps may be sufficient to evaluate the conversion gain, making this method much faster. Also, through the subtraction of the ramps, it allows to get rid of the fixed pattern noise. Then the spatial mean and the spatial variance are derived for each frame of the ramp as

$$S = \text{mean} \left(\frac{S_1 + S_2}{2} \right), \quad (3)$$

$$\sigma_S^2 = \text{variance} \left(\frac{S_2 - S_1}{2} \right), \quad (4)$$

where *mean* and *variance* are taken over a chosen area of pixels and S_1 and S_2 are obviously the signals in the two ramps respectively.

In any case, the calculation requires proper selection of pixels to avoid non-linear pixels, as described in more details in 3.2, and choice of incoming fluxes and ramp length to remain within the linear regime of the detector. Part 3.3 shows how telemetry gives us evidence of the quality of the data taken, while part 3.4 gives some results and compares gains obtained for different configurations.

3.2 Pixel selection

Since signal and noise are calculated over a group of pixels, respectively as their mean and variance values, it is important to exclude pixels whose signal or noise, for some reason, lies in the tail of the distribution. A simple $5\text{-}\sigma$ cut would lead to a proper result but is nevertheless not satisfying in that it has no physical meaning. Consequently, our selection of pixels has followed several criteria:

1. remove disconnected pixels: basically, this excludes a few hundreds of pixels
2. remove pixels with high baseline (over 30,000 ADU), as we want to work in the linear regime: another few hundreds of pixels excluded
3. remove non-linear pixels with a Quality Factor on the linearity of the ramp
4. aggregate pixels according to their interpixel capacitance (IPC) value which modifies the gain

Selection with regard to linearity

Beyond selecting a proper range of fluxes, some pixels appear to have a strong non-linearity, whatever the flux. Non-linearity has been evaluated thanks to a quality factor (QF) based on χ^2 calculations. This quality factor is described in details elsewhere.¹¹ It is derived for each ramp and each pixel with a view to validating the calculated flux. Figure 4, left, shows the normalized histogram of QF for scs2 for an incoming flux of 52 e/s.[†] The width of the peak depends on the incoming flux and gets larger with higher fluxes. A very long tail may also be observed that definitely needs to be cut, as it corresponds to highly non-linear pixels. A cut on QF beyond 10 has thus been applied to all ramps.

Selection with regard to IPC

Interpixel capacitance (IPC) has been measured thanks to the Single Pixel Reset (SPR) technique.⁹ IPC histogram of scs2 seen in figure 4, center, shows three peaks: the main one, on the left, corresponds to the majority of pixels ; the second peak, to the right, includes pixels with lower IPC and the third peak corresponds to boundary pixels between those two regions. Thus, two regions may be defined with “low” and “high” IPCs. The difference is actually due to the process of fabrication taking place during the “gluing” of the sensitive MCT area onto the indium bumps. These two regions will turn out, as seen below, to have rather different conversion gains and should thus be treated separately.

[†]52 e/s is the LED setpoint, the actual flux might be slightly different.

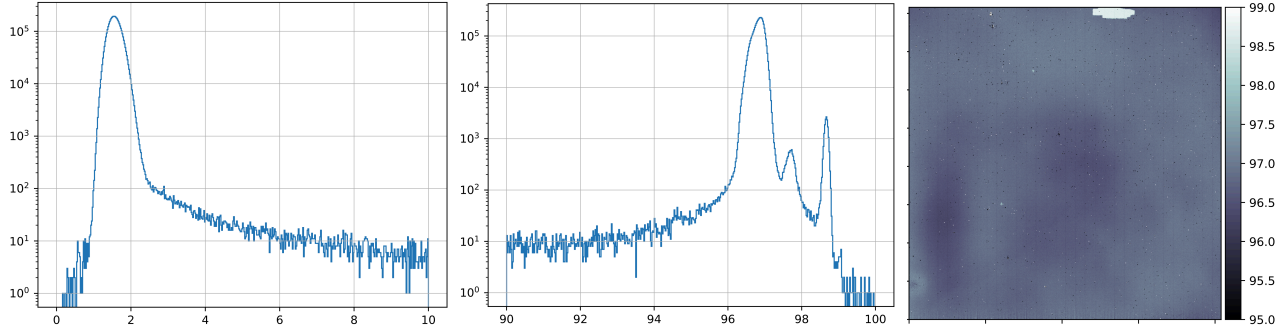


Figure 4. Normalized QF histogram [left], IPC histogram [center] and map [right] for scs2.

3.3 Telemetry

Euclid firmware, loaded in the SCE, provides powerful analog telemetry. Each frame coming from the cold readout electronics (SCE) contains an additional column sheltering digitized values of main bias voltages and currents, temperature sensors and logical states of the SCE. This allows us to verify, on an almost real time basis, the overall system stability.

The preamp gain for bias voltages is of -3dB (0.707) giving a resolution of about $80 \mu\text{V}/\text{ADU}$. Figure 5, left, displays the histogram of the main analog voltage VDDA over a 12 hour acquisition (i.e. 27000 frames). Notice that the stability of the voltage (even combined with the readout noise of the system) given by the RMS of the distribution is of 0.3 mV (0.1%).

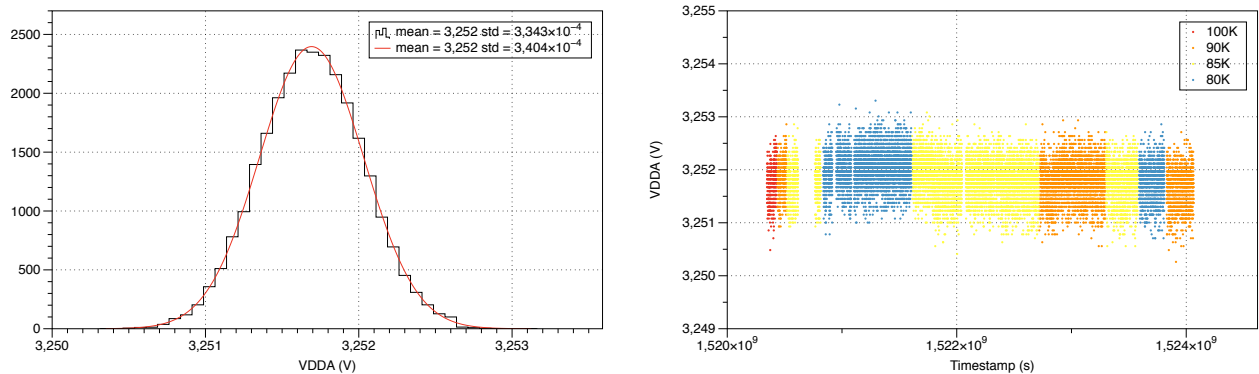


Figure 5. Histogram of VDDA over a 12 hour acquisition [left] and chronogram of VDDA over the whole characterization flow (45 days) [right]. Colors show the changing temperatures.

The chronogram of the same voltage for all runs of a detector full characterization, that is over 45 days of acquisition, combining the four temperatures, is given in figure 5, right. Again, the bias value digitized by the SCE is very stable, which is a good indicator of the goodness of data taken.

3.4 Mean gain

After initially working over the whole matrix to which the above described pixel selection has been applied, smaller areas have been chosen (channels, columns, pixels), which requires many data in order to obtain acceptable statistical error on the resulting gain. Various results are presented in figure 6 and detailed hereafter. Part 3.5 is dedicated to the per pixel conversion gain measurement method itself.

Gain vs. ramp length

While, in the general case, the conversion gain is expected to be constant, we took a look at its variation with the length of the ramp (in other words the integrated incoming signal). For that matter, we applied the mean variance method and calculated the conversion gain on partial ramps of N frames (namely selecting frames from first frame to frame N) and varying N from 10 to 400, the total length of the acquired ramps. The derived conversion gain is plotted against the number N of selected frames in figure 6, for various configurations. Some discrepancies may be seen, most probably a consequence of persistence and this issue should be explored further. The gain has been calculated over 20 ramps of continuous illumination acquired at 52 e/s incoming flux. Error bars shown in figure 6 are calculated from the standard deviation of all 19 pairs of ramps.

First let us look at the black curve on the left for which the whole matrix and the whole ramp were used, with reference pixel correction (as mentioned above). It may be observed, as expected, that the statistical error is larger at the beginning of the ramp where the readout noise is dominating. Similarly, at larger signals (end of ramp) the decreasing slope is due to the non-linearity of the detector, which thus seems to start already at the 100th frame, namely around 5000 ADU.

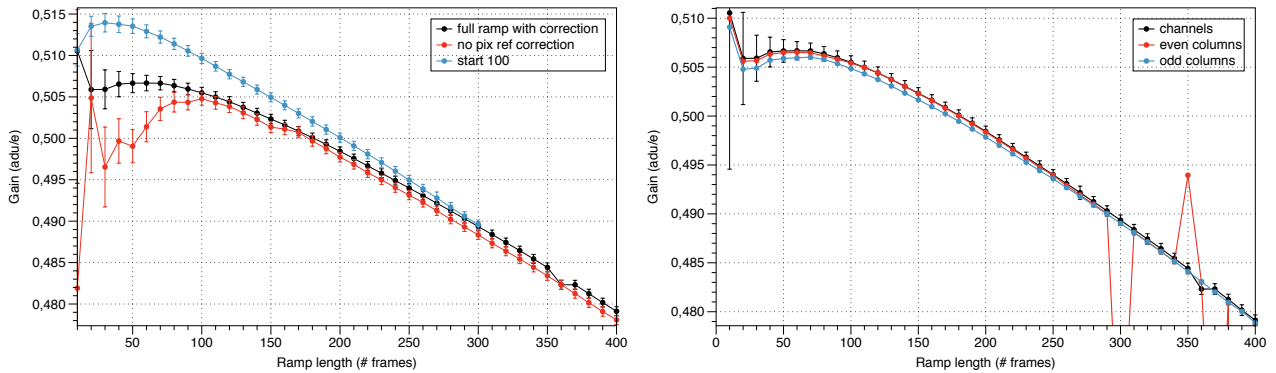


Figure 6. Conversion gain calculated over the length of the ramp for three configurations: full ramp with pixel correction, full ramp without pixel correction, and starting ramp at frame 100 [left]. Comparison of conversion gain for three subsets of pixels: channels, odd columns and even columns [right]

Reference pixel correction

In comparison to the black curve, the red curve shows the gain obtained with no reference pixel correction. Clearly, both red and black curves show the same slope of non-linearity. However, there is a strong effect at the beginning of the ramp that shows that spatial variance contains more than shot noise. Reference pixel correction improves the accuracy and reduces systematic errors due to correlations.

Start of ramp

The blue curve is obtained with reference pixel correction, but after removing the first 100 frames. As expected the new beginning of the ramp is then much neater and the slope of the non-linearity still the same.

Odd and even columns

In figure 6, right, we compare three subsets of pixels: channels, odd columns and even columns. For each subset, conversion gain is initially derived for individual channel or column and then an average value for all columns or all channels is represented in figure 6. Error bars are calculated over centered gains from all subsets over the 19 values obtained. Thus the values obtained give a maximum error since it includes the actual error plus the RMS of the distribution of all values in the subset. Some discrepancies may be seen, most probably due to outliers that have not been rejected by our quality factor. This should be looked into in order to find more efficient selection criteria.

Finally, even columns and channels are almost superimposed, while odd columns are very slightly off. No effect seems connected to the channel output buffer. Odd and even columns have different current sources and the slight variation could be connected to different clocking.

3.5 Gain per pixel

If scs2 has been chosen for calculations over the matrix, allowing to exclude very few pixels (less than 0.8%, including the “IPC” area), it is more interesting to work here with scs1 which shows a larger “IPC” area that will be hereafter referred to as the “Fish”. In order to observe spatial variations of the gain and to be sure to get enough statistics:

1. reference pixel correction has been applied to all pixels,
2. pixel selection has been applied as described above, but both “IPC” areas have been included here,
3. pixels have been grouped into larger pixels composed of 16x16 pixels, or 64x64 pixels,
4. the length of the ramps has been limited to 5000 ADU integrated flux so as to limit non-linearity effects,
5. many acquisitions taken at incoming fluxes varying from 4 e/s up to 52 e/s have been combined together to increase the statistics.

Again the conversion gain is obtained from the “fast PTC” technique fitting the variance vs. signal ramp obtained from the combination of numerous ramps limited to an integrated signal of 5000 ADU. The combination of ramps from various fluxes seems natural, as seen in figure 3. However the combination of acquisitions of various types is not that obvious. Indeed, figure 7 shows three maps with 16x16 pixels grouping for the three types of acquisitions. The Fish distinctly comes out with a gain 5% higher than the rest of the map. But the background of the “flux” acquisition is quite different from the two others and may be understood looking at figure 8. Indeed, the latter figure shows the 20 ramps cumulated for an incoming flux of 52 e/s. The beginning of the “flux” ramps shows a decrease, synonymous of detrapping, while the two other types of ramps “zodi” and “dark” start by increasing, synonymous of charge trapping. Consequently, “zodi” and “dark” acquisitions may be combined together, but not with “flux”. As a result (not shown here), even if this combination of ramps gives an error on the gain smaller than 1%, the spatial variations of the gain are still embedded in noise.

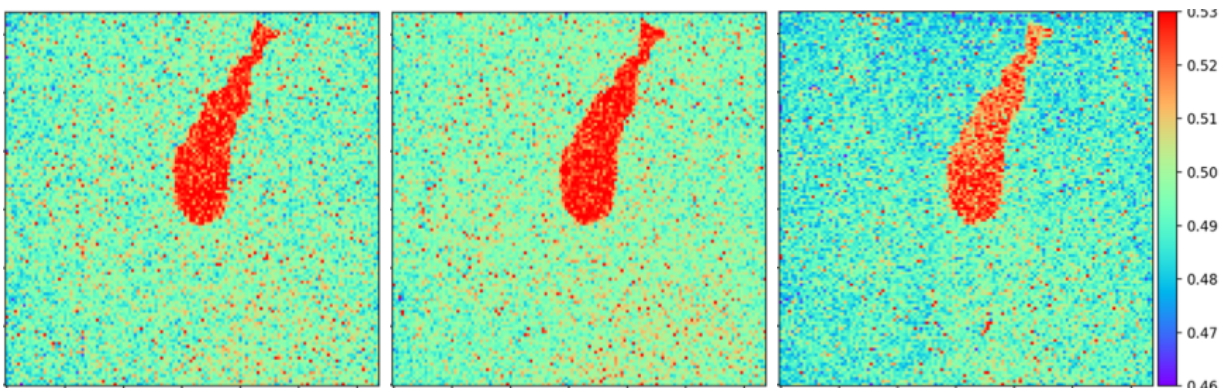


Figure 7. Maps of pixel gains obtained for super pixels of 16x16 pixel area for the three types of acquisitions: flux zodi [left], flux dark [center], flux [right]

A first sight of a 64x64 pixels map of the conversion gain is given in figure 9 with a view to getting a better insight into spatial variations. Conversion gain has been calculated from 170 values of gain. Figure 9, left, represents the distribution of all the 64x64 pixels, where the secondary peak of the Fish sticks out. Both peaks of the histogram show an RMS error of 0.53% which combines the dispersion of the super pixel gains and an error of 0.26% on the super pixel conversion gain (as calculated from the 170 values of gain obtained for each

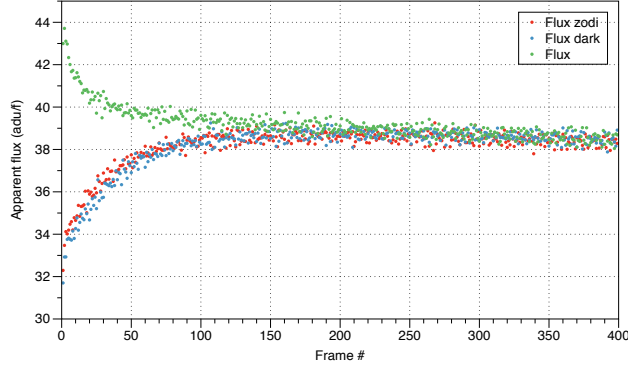


Figure 8. Ramps for 52e/s LED setpoint are shown for the different types of acquisitions. One may see the different behaviors of the detector according to history of illumination.

pixel). At this level of error, one can start to see the spatial variations of the gain as seen in figure 9, right: the lower right area clearly tends to be redder, thus higher gains, while the left of the matrix tends to bluer colors, or smaller gains. The variations are very small (less than 1%) but should be taken into account for the Euclid mission.

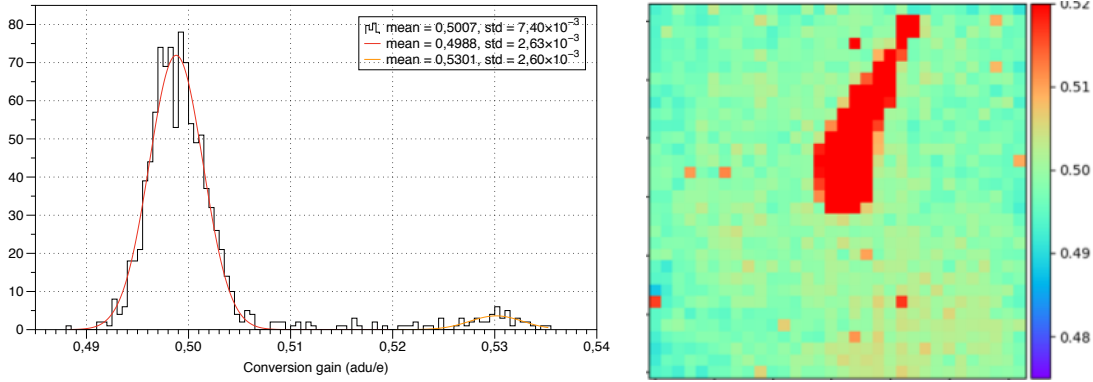


Figure 9. Per pixel conversion gain of scs1 for 64x64 pixels showing their distribution [left] and the gain map [right]

It has been mentioned above (3.2) that what differentiates the Fish and the background is their IPC. Other authors have indeed mentioned the necessity to correct for IPC in order to get a proper estimation of the conversion gain.^{10,12} Indeed IPC modifies the pixel capacitance by adding a parasitic capacitance. If we compare the image of figure 9 with the IPC image we obtained by SPR technique, the gain difference between the Fish area and the rest of the detector is roughly compatible with the coefficient $1 - 8\alpha$ (where α is the coupling coefficient over four adjacent pixels) given in literature.

4. CONCLUSION AND FUTURE WORK

We have presented in this paper the setup and first results on the characterization of the Euclid flight H2RG detectors done at CPPM since June 2017. We have focused on the conversion gain, which is a fundamental parameter essential to evaluate actual fluxes in terms of incident photons. It has been seen to be influenced by many aspects: spatial variations along pixels or columns (at a smaller degree), IPC, and history of illumination (following trapping or detrapping in link with persistence effect). A conversion gain map with “super pixels” of 64x64 pixels has been produced showing not only that spatial variations become visible with an error smaller than 1%, but also that a small scale (16x16 pixel or smaller) map of the detector conversion gain is attainable and should be derived for the purpose of the science mission. In order to get a better map, to the single pixel

level, it will be necessary to improve statistics by combining more acquisitions and to apply a finer selection of pixels. Correction of non-linearity and IPC would certainly improve the quality of the data and thus the measurement of the conversion gain.

ACKNOWLEDGMENTS

Thanks to EC collaboration. Project funded by CNES and ESA. Thanks also to NASA Goddard and JPL for fruitful discussions. Special thanks to Augustyn Waczynski with whom we had a close collaboration working on acceptance tests at DCL.

REFERENCES

- [1] Laureijs, R., Amiaux, J., Arduini, S., Auguères, J., Brinchmann, J., Cole, D., Cropper, M., Dabin, C., Duvet, L., Ealet, A., et al., “Euclid definition study report,” tech. rep., ESA (2011).
- [2] Maciaszek, T. et al., “Euclid near infrared spectrometer and photometer instrument concept and first test results obtained for different breadboards models at the end of phase c,” in [*Space Telescopes and Instrumentation: Optical, Infrared, and Millimeter Wave*], *Proc. of SPIE* **9904**, 99040T (2016).
- [3] Secroun, A., Serra, B., Clémens, J.-C., Ealet, A., Lagier, P., Legras, R., Niclas, M., Caillat, L., Gillard, W., Tilquin, A., Barbier, R., Ferriol, S., Kubik, B., Smadja, G., Prieto, E., Masciazek, T., and Sorensen, A. N., “Characterization of h2rg ir detectors for the euclid nisp instrument,” in [*Space Telescopes and Instrumentation: High Energy, Optical, and Infrared Detectors for Astronomy*], *Proc. of SPIE* **9915**, 99151Y (2016).
- [4] Kubik, B., Barbier, R., Castera, A., Chabanat, E., Ferriol, S., and Smadja, G., “Impact of common modes correlations and time sampling on the total noise of a h2rg near-ir detector,” in [*Space Telescopes and Instrumentation: High Energy, Optical, and Infrared Detectors for Astronomy VI*], *Proc. of SPIE* **9154**, 91541B–1–13 (2014).
- [5] Janesick, J., Kalassen, K., and Elliott, T., “Ccd characterization using the photon transfer technique,” *Proc. of SPIE* **570**(7-19) (1985).
- [6] Janesick, J., [*Photon Transfer: $DN \rightarrow \lambda$*], vol. PM170, Spie Press Book (2007).
- [7] Holdsworth, D. W., Gerson, R. K., and Fenster, A., “A time-delay integration charge-coupled device camera for slot-scanned digital radiography,” *Med. Phys.* **17**, 876–886 (1990).
- [8] Bohndiek, S. E., Blue, A., Clark, A. T., Prydderch, M. L., Turchetta, R., Royle, G. J., and Speller, R. D., “Comparison of methods for estimating the conversion gain of cmos active pixel sensors,” *IEEE Sensors Journal* **8**(10), 1734–1744 (2008).
- [9] Finger, G., Beletic, J. W., Dorn, R., Meyer, M., Mehrgan, L., Moorwood, A. F. M., and stegmeier, J., “Conversion gain and interpixel capacitance of cmos hybrid focal plane arrays,” *Experimental Astronomy* **19**, 135–137 (2005).
- [10] Moore, A., Ninkov, Z., and Forrest, W., “Interpixel capacitance in non-destructive focal plane arrays,” in [*Focal Plane Arrays for Space Telescopes*], *Proc. of SPIE* **5167**, 204–215 (2003).
- [11] Kubik, B., Barbier, R., Chabanat, E., Chapon, A., Clémens, J.-C., Ealet, A., Ferriol, S., Gillard, W., Secroun, A., Serra, B., Smadja, G., and Tilquin, A., “A new signal estimator from the nir detectors of the euclid mission,” *Publications of the Astronomical Society of the Pacific* **128**(968), 104504 (2016).
- [12] Fox, O., Waczynski, A., Wen, Y., Foltz, R., Hill, R., Kimble, A., Malumuth, E., and Rauscher, B., “The 55fe x-ray energy response of mercury cadmium telluride near-infrared detector arrays,” *Publications of the Astronomical Society of the Pacific* **121**(881), 743–754 (2009).